Modeling solar wind mass-loading in the vicinity of the Sun using 3-D MHD simulations

A. P. Rasca,[1,2] M. Horányi,[1,3] R. Oran,[4] and B. van der Holst[4]

Received 27 August 2013; revised 30 November 2013; accepted 10 December 2013; published 13 January 2014.

[1] Collisionless shocks due to mass-loading were first discussed to describe the solar wind flow around a cometary atmosphere, showing its choking effects on the flow. Recent observations have led to an increased interest in mass-loading occurring in the solar corona due to both sungrazing comets and collisional debris production by sunward migrating interplanetary dust particles. The 1-D simulations with a hydrodynamic model have illustrated the impact on the solar wind from abrupt mass-loading in the coronal region. Full 3-D magnetohydrodynamic (MHD) simulations using a solar corona model based on the Block-Adaptive-Tree-Solarwind-Roe-Upwind-Scheme code provide a more realistic coronal environment for modeling specific events applicable to modeling the mass-loaded coronal wind. A specific application is introduced modeling the mass-loading effects from a sungrazing comet.

Citation: Rasca, A. P., M. Horányi, R. Oran, and B. van der Holst (2014), Modeling solar wind mass-loading in the vicinity of the Sun using 3-D MHD simulations, *J. Geophys. Res. Space Physics*, *119*, 18–25, doi:10.1002/2013JA019365.

1. Introduction

[2] The dynamics of charged dust particles picked up by the solar wind and other plasma environments is a growing area of interest, with several future space missions still focusing on exploring dusty plasma environments. This is in addition to past and present work observing and modeling dusty plasma environments around planetary objects such as the moon, planetary rings, and comets [*Horány*, 1996]. Specifically, current missions such as the New Horizons and the Cassini-Huygens space probes, where dust-detector instruments are helping build a better picture of the dust environments in the solar system [*Horányi et al.*, 2008]. Additionally, a number of planned missions such as the Lunar Atmospheric and Dust Environment Explorer are set to explore the dusty plasma environment around the moon [*Grün et al.*, 2011].

[3] Current exploration of dusty plasma environments omits charged dust particles from the dust cloud occupying the F-corona near the Sun. However, there are theoretical studies modeling the size, density, distribution, and trajectories of dust particles migrating in toward the Sun [*Mann and MacQueen*, 1996], which can then be ejected as β-meteoroids. Dust particles can reach the coronal region via larger bodies such as sungrazing comets, which release dust and gas on approach to the Sun. Upon being ionized, these particles can eventually be detected downstream by space probes such as the STEREO/WAVES instrument [*Meyer-Vernet et al.*, 2009].

[4] Plans to explore the solar corona and take direct measurements provide a great opportunity for further theoretical modeling of the coronal dusty plasma environment. One particular mission of interest is Solar Probe Plus, which will launch in 2018 and spend 7 years orbiting the Sun, with one approach $8.5\,R_{\odot}$ from the solar surface. Solar Probe Plus will be able to sample the solar corona and explore the corona's dusty plasma environment. Modeling data provide examples of how a dust source footprint may appear to such a solar probe.

[5] A study by *Rasca and Horányi* [2013] introduces a simple 1-D hydrodynamic (HD) model showing effects on the solar wind due to pickup ions from the F-corona. They presented a number of steady state solutions resulting from sudden bursts of micron-sized dust particles at varying distances from the Sun. The modeled mass-loaded wind behaves much like a compressible fluid flowing through a de Laval nozzle. A sudden wind acceleration was observed in the regions where dust is being picked up by the solar wind, and depending on whether the solar wind supersonic or subsonic, a shock or deceleration precedes the acceleration, respectively, in addition to a general jump in the mean particle mass (Figure 1).

[6] The work done by *Rasca and Horányi* [2013] is based on a purely HD model. Though their study is meant to be a very simplified example of how mass-loading in the solar corona affects the acceleration and composition, there are a few known disadvantages. The primary disadvantage of using the HD model is the lack of consideration of

[1]Laboratory for Atmospheric and Space Physics, University of Colorado Boulder, Boulder, Colorado, USA.
[2]Department Applied Mathematics, University of Colorado Boulder, Boulder, Colorado, USA.
[3]Department of Physics, University of Colorado Boulder, Boulder, Colorado, USA.
[4]Department of Atmospheric, Oceanic and Space Sciences, University of Michigan, Ann Arbor, Michigan, USA.

Corresponding author: A. P. Rasca, University of Colorado Boulder, 1234 Innovation Dr., Boulder, CO 80303, USA. (rasca@colorado.edu)

2169-9380/14/10.1002/2013JA019365

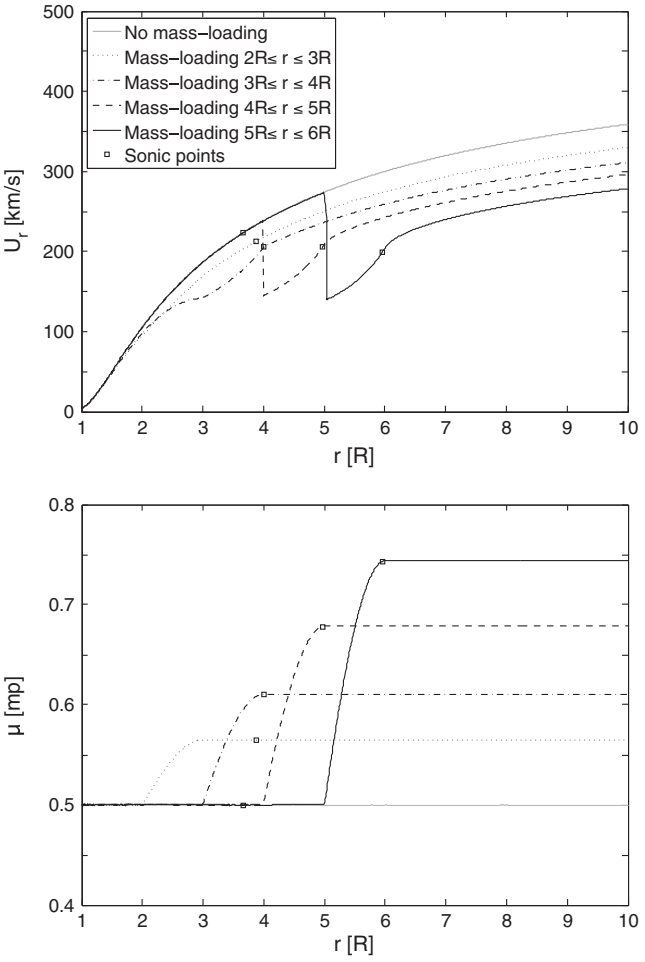

Figure 1. Steady state solutions for radial velocity and mean molecular weight from *Rasca and Horányi* [2013] with mass-loading occurring in four different spacial intervals away from the Sun. The sonic points for both the undisturbed solar wind and the new steady states are marked. Reprinted with permission from *Rasca and Horányi* [2013].

magnetic field effects, particularly the inclusion of magnetic pressure. We will apply the same mass-loading model to a full 3-D magnetohydrodynamic (MHD) coronal wind model based on the Block-Adaptive-Tree-Solarwind-Roe-Upwind-Scheme (BATS-R-US) code developed at the University of Michigan's Center for Space Environment Modeling (CSEM).

[7] In the next section we will discuss the 1-D HD model used for mass-loading in the solar corona. In section 3 we will introduce the 3-D MHD solar corona model as a solar wind modeling tool for our mass-loading problem. Section 4 will have us comparing our 1-D HD results with new 3-D MHD to confirm that we get similar results with a shock-generating mass-loading region. In our last two sections we will introduce an application of the model for sungrazing comets and discuss future work.

2. Coronal Mass-Loading Model Description

[8] *Rasca and Horányi* [2013] looked at a hydrodynamic solar wind model with a mass-loading model introduced by *Biermann et al.* [1967] in the context of cometary ions. The model used by *Biermann et al.* [1967] was an axially symmetric system of HD equations with source terms $\mathbf{S_d} = (S_{d1}, S_{d2}, S_{d3})^\top$ for mass-loading, but for a spherically symmetric coronal wind the 1-D (in space) set of equations

$$\frac{\partial(A\rho)}{\partial t} + \frac{\partial(A\rho u)}{\partial r} = AS_1 \tag{1}$$

$$\frac{\partial(A\rho u)}{\partial t} + \frac{\partial(A\rho u^2)}{\partial r} + A\frac{\partial p}{\partial r} = AS_2 \tag{2}$$

$$\frac{\partial(AE)}{\partial t} + \frac{\partial}{\partial r}[Au(E+p)] = AS_3 \tag{3}$$

were used, where the dependent variables ρ, u, and p are used as the solar wind mass density, radial flow velocity, and pressure, respectively, with the constant γ being the adiabatic index, defined as $\gamma = 5/3$ in this case. E is the total energy defined as

$$E = \rho\left(\frac{1}{2}u^2 + \frac{p}{\rho(\gamma-1)}\right) \tag{4}$$

and A is the spherical area expansion $A = r^2$. For a coronal wind, the mass, momentum, and energy sources $\mathbf{S} = (S_1, S_2, S_3)^\top$ need to include not just mass-loading sources $\mathbf{S_d}$ but gravitational and energy transfer (conductive and radiative) sources as well.

[9] The mass-loading terms $\mathbf{S_d}$ are used to take into account changes in the solar wind when particles are ionized and have their mass, momentum, and energy added to the flow. *Biermann et al.* [1967] focused on three primary modes of ionization: photoionization, charge exchange, and electron impact. Mass-loading by photoionization means the mass, momentum, and energy the particles had beforehand is simply added to the system. For the other two modes of ionization, interactions with particles already in the flow make calculating the source contributions less trivial. Fortunately, at the heliospheric distances we use both charge exchange and electron impact become negligible relative to photoionization, allowing the dust source terms $\mathbf{S_d} = (S_{d1}, S_{d2}, S_{d3})^\top$ to be defined using only the photoionization process,

$$S_{d1} = P_d\rho_d \tag{5}$$

$$S_{d2} = P_d\rho_d u_d \tag{6}$$

$$S_{d3} = \frac{1}{2}P_d\rho_d u_d^2, \tag{7}$$

where P_d, ρ_d, and u_d are the neutral dust ionization rate, mass density, and velocity, respectively. Occasionally, $P_d\rho_d$ will be seen represented by $P_{ml} = P_d\rho_d$, the mass-loading rate per volume, since the ionization rate and mass density appear frequently together. We can also make a simplification in equations (5)–(7) if u_d is sufficiently smaller in magnitude than the solar wind velocity. In this case it can be assumed that the neutral dust is approximately stationary in the radial direction, leading to the mass source that is the primary influence on the flow due to dust.

[10] Also, *Rasca and Horányi* [2013] discussed an equation for effective area A_{eff}, based on a derivation by *Gombosi et al.* [1986] for dust and gas interactions in a cometary atmosphere, to help illustrate choking and

dispersing nozzle effects each source has on the solar wind flow

$$\frac{1}{A_{\rm eff}}\frac{dA_{\rm eff}}{dr} = \frac{A'}{A} - \frac{\gamma+1}{2\gamma}\frac{u}{p}S_1 + \frac{1}{p}S_2 - \frac{\gamma-1}{\gamma}\frac{1}{pu}S_3. \quad (8)$$

For $S_{d1} \geq 0$ and $S_{d2} = S_{d3} = 0$ in equation (8) there is a convergent (or choking) nozzle effect which decelerates supersonic flows and accelerate subsonic flows. This is shown very effectively in the bottom two curves in Figure 1 (left), where the wind does not hit a mass-loading region until after the sonic point. The mass-loading term causes sudden deceleration resulting in a shock, followed by reaccelerating as a subsonic flow.

[11] Being 1-D HD, this is a fairly simplified model of the coronal wind. While the actual solar wind does behave much like a fluid, it is also made up of charged particles mutually interacting with solar-originating magnetic fields. The lack of magnetic fields **B** in a purely HD model reflects the magnetic pressure component. The total pressure should be the sum of the gas pressure and magnetic pressure,

$$p = p_{\rm gas} + p_{\rm mag}, \quad (9)$$

but the HD model only includes the gas pressure $p = p_{\rm gas}$. Additionally, this model is restricted to one dimension, even though it does capture the generally spherical geometry of the flow. Hence, we cannot see how the magnetic field environment is changing in a 3-D space due to the mass-loaded solar wind. For these reasons we will apply the same mass-loading model to a 3-D MHD code.

3. MHD Model Description

[12] We have implemented a 3-D MHD version of the solar wind mass-loading model discussed in the previous section using the Solar Corona (SC) component of the Solar Weather Modeling Framework (SWMF), developed at the University of Michigan's Center for Space Environment Modeling (CSEM). Several components of the SWMF, including SC, use the BATS-R-US code, which is a massively parallel MHD code using a finite volume upwind solver, and include adaptive mesh refinement (AMR) for resolving regions of high gradients such as the coronal base and current sheet. Both BATS-R-US and the SWMF are described in *Tóth et al.* [2012, and references therein].

[13] In the current study, we build on the coronal model of *van der Holst et al.* [2010] for the SC component. This model solves the coupled system of the MHD equations and Wentzel-Kramers-Brillouin for low-frequency Alfvén waves. The waves serve to accelerate and heat the plasma in open magnetic field lines [*Hollweg*, 1986]. Although this model is capable of describing a two-temperature (electrons + protons) plasma, in this work we consider a single-temperature plasma, since we wish to focus on the plasma-dust interaction. For this purpose, we modified the van der Holst model to account for dust-wind interactions through mass-loading by extending it to a multispecies description. The multispecies capabilities of BATS-R-US are described in *Tóth et al.* [2012]. The multispecies aspect generates an additional mass conservation equation as a result of splitting the mass density into hydrogen density $\rho_{\rm H}$ (both protons and electrons) and ionized dust density ρ_{d_i},

$$\rho = \rho_{\rm H} + \rho_{d_i}. \quad (10)$$

[14] The full set of MHD equations become

$$\frac{\partial \rho_{\rm H}}{\partial t} + \nabla\cdot(\rho_{\rm H}\mathbf{u}) = 0 \quad (11)$$

$$\frac{\partial \rho_{d_i}}{\partial t} + \nabla\cdot\left(\rho_{d_i}\mathbf{u}\right) = S_{\rho_{d_i}} \quad (12)$$

$$\frac{\partial(\rho\mathbf{u})}{\partial t} + \nabla\cdot\left[\rho\mathbf{u}\mathbf{u} + \left(p + p_{\rm W} + \frac{B^2}{2\mu_0}\right)I - \frac{\mathbf{B}\mathbf{B}}{\mu_0}\right] = \mathbf{S}_{\rho\mathbf{u}} \quad (13)$$

$$\frac{\partial \mathbf{B}}{\partial t} + \nabla\cdot(\mathbf{u}\mathbf{B} - \mathbf{B}\mathbf{u}) = 0 \quad (14)$$

$$\frac{\partial E}{\partial t} + \nabla\cdot\left[\mathbf{u}\left(E + p + p_{\rm W} + \frac{B^2}{2\mu_0}\right) - \frac{(\mathbf{u}\cdot\mathbf{B})\,\mathbf{B}}{\mu_0} + \left(E_{\rm W}^{+} - E_{\rm W}^{-}\right)\mathbf{u}_{\rm A}\right] = S_E, \quad (15)$$

where B, μ_0, and $\mathbf{u}_{\rm A}$ are the magnetic field strength, permeability of free space, and Alfvén speed, respectively. The wave energy densities of the Alfvén waves propagating parallel and antiparallel to **B** are denoted by $E_{\rm W}^{+}$ and $E_{\rm W}^{-}$, respectively, and the Alfvén wave energy density and pressure are defined as

$$E_{\rm W} = E_{\rm W}^{+} + E_{\rm W}^{-} \quad (16)$$

and

$$p_{\rm W} = E_{\rm W}/2. \quad (17)$$

Also, $B^2/2\mu_0$ is the magnetic pressure absent in the previous section, while the gas pressure p remains as the sum of hydrogen and dust pressures. The energy definition is modified from the purely HD definition in equation (4) to

$$E = \frac{1}{2}\rho u^2 + \frac{p}{\gamma-1} + \frac{B^2}{2\mu_0} + E_{\rm W}, \quad (18)$$

with the Alfvén wave energy given by the time-dependent solution of

$$\frac{\partial E_{\rm W}^{\pm}}{\partial t} + \nabla\cdot\left[E_{\rm W}^{\pm}(\mathbf{u} \pm \mathbf{u}_{\rm A})\right] = -p_{\rm W}^{\pm}\nabla\cdot\mathbf{u} - Q^{\pm}, \quad (19)$$

where the $\pm$ sign stems from two Alfvén wave solutions. $Q^{\pm}$ is the wave dissipation defined as

$$Q^{\pm} = \frac{\left(E_{\rm W}^{\pm}\right)^{3/2}}{L\sqrt{\rho}}, \quad (20)$$

where L is the perpendicular correlation length of the Alfvén waves. The nonzero source terms for mass, momentum, and energy take into account mass-loading, gravity, thermal heat flux, and angular motion of the Sun,

$$S_{\rho_d} = S_{d1} \quad (21)$$

$$\mathbf{S}_{\rho\mathbf{u}} = \mathbf{S}_{d2} - \rho\left[\frac{GM}{r^3}\mathbf{r} + \boldsymbol{\Omega}\times(\boldsymbol{\Omega}\times r) + 2\boldsymbol{\Omega}\times\mathbf{u}\right] \quad (22)$$

$$S_E = S_{d3} - \nabla\cdot\mathbf{q} - \rho\mathbf{u}\cdot\left[\frac{GM}{r^3}\mathbf{r} + \boldsymbol{\Omega}\times(\boldsymbol{\Omega}\times\mathbf{r})\right]. \quad (23)$$

G is the gravitation constant, M is the solar mass, **q** is the Spitzer thermal heat flux vector applied within $10\,R_\odot$, and $\boldsymbol{\Omega}$ is the angular velocity of the Sun.

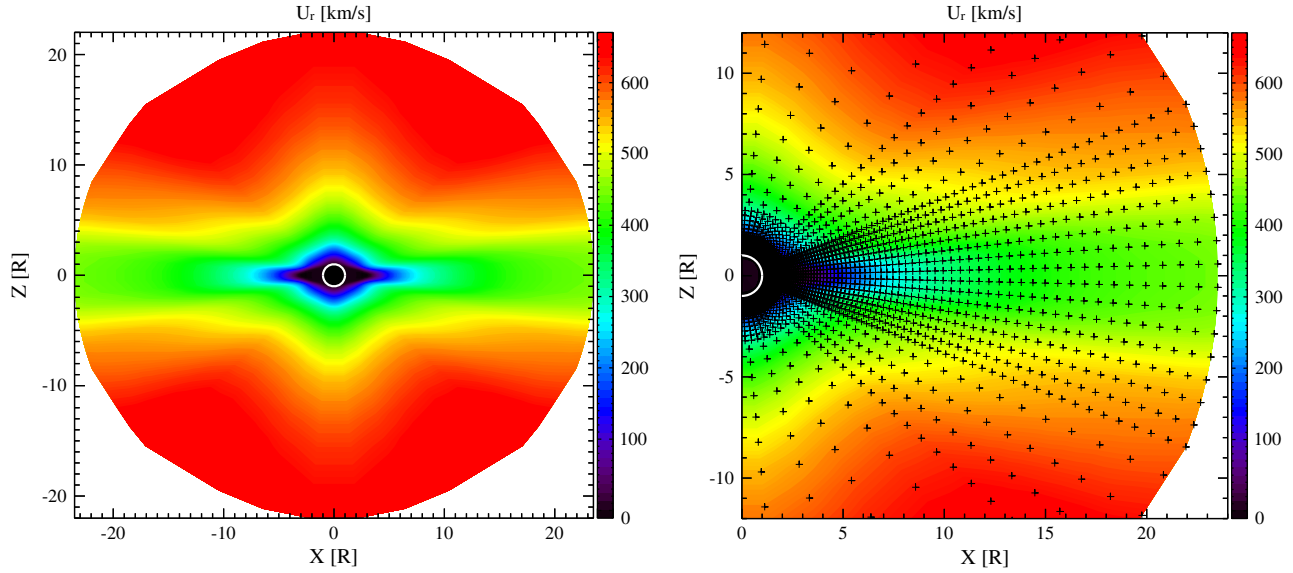

Figure 2. The radial velocity steady state in (left) the *xz* plane from solving the SC component (equations (11)–(15)) and (right) the computational grid used with initial AMR regions near the Sun and encompassing the current sheet.

[15] A spherical grid is used for the SC component, where the inner boundary is defined at the coronal base and the outer boundary defined at $r = 24\,R_\odot$. This limits how far downwind we can model in this study, but the Inner Heliosphere component of the SWMF couples with the SC component for potentially extending the domain in further studies. The inner boundary for the magnetic field uses the solar dipole field at $1\,R_\odot$ with field strength $1.4\,G$ at the poles, while the remaining inner boundary values are determined using the Wang-Sheely-Arge model [*Arge and Pizzo*, 2000], with the temperature and number density normalized to 1.5×10^6 K and 10^8 cm^{-3} at the coronal base. The radial distance for the outer boundary can be arbitrarily chosen, provided the wind speed at the boundary exceeds the fast magnetosonic speed, for outflow boundary conditions, which is satisfied well below $r = 24\,R_\odot$. The grid uses a $6 \times 4 \times 4$ block tree structure, meaning the entire grid in a collection of blocks with dimensions $6 \times 4 \times 4$ cells in the radial, polar, azimuthal directions, respectively. As the grid is refined using AMR, target blocks are divided into eight smaller blocks with the same cell structure. Some refinement is used near the inner boundary, which is located above the transition region, making a fine grid resolving the sharp gradients unnecessary.

[16] The general 3-D structure of the solar wind, without the inclusion of the mass-loading source terms is illustrated in Figure 2, where we show results from a steady state (in the corotating frame) simulation. Color contours show the radial speed in the entire domain (Figure 2, left), and a zoomed-in version with the computation grid overlaid (Figure 2, right), with the refined blocks being near the inner boundary and at the current sheet. Unlike the 1-D model, the 3-D solar wind has a latitude-dependent structure. A fast wind blows above the poles, while a slow wind occupies the equatorial regions. The 1-D wind model is based on slow wind parameters, which is evident when observing the radial velocities from Figure 2 along the *x* axis (Figure 3).

4. Comparing 1-D HD Results With MHD Simulations

[17] The purpose of the 1-D results discussed in section 2 are to illustrate the outcome of a mass-loaded solar wind in the corona, and the 1-D aspect does allow for a simple and convenient model to work with, but a full 3-D MHD solar wind gives a better picture of the environment being mass-loaded. Two major resulting differences with the slow wind velocity profile depicted in Figure 3 from the undisturbed wind velocity in Figure 1 (left), while similar in shape and velocity, are the outward shift of initial acceleration from a near-zero wind and the sonic point, each now located at around $3\,R_\odot$ and $5\,R_\odot$, respectively. These differences affect how we will set up simulations for comparing 3-D MHD results with the 1-D HD results.

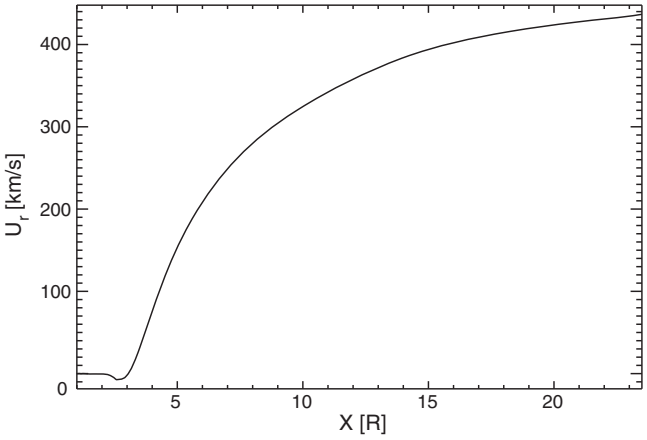

Figure 3. The radial velocity steady state from Figure 2 depicted along the *x* axis. Due to symmetry from our boundary conditions, the radial velocity profiles should be equal in any radial direction in the *xy* plane.

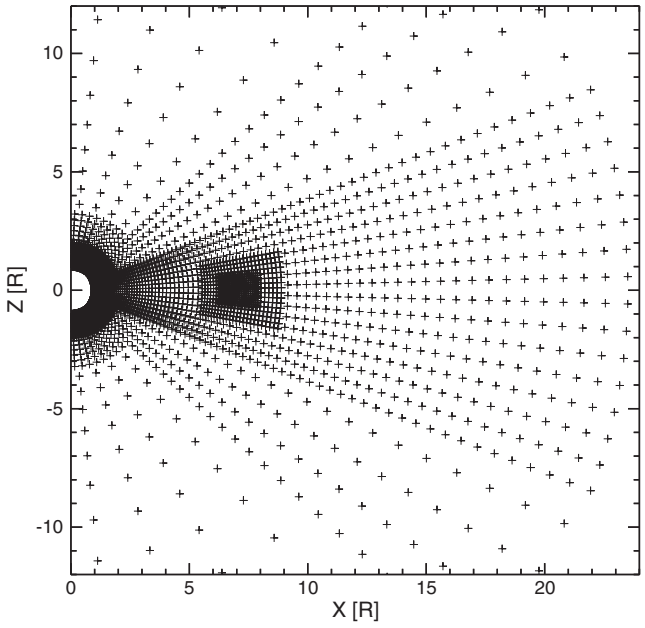

Figure 4. The spatial grid in the *xz* plane used for the postsonic point case, with a *z*-centered AMR region encompassing the mass-loading region.

[18] To compare mass-loading results between using 1-D HD and 3-D MHD models, we need to change the location of our mass-loading region. The shock-generating mass-loading regions in Figure 1 are placed just downstream of the sonic point. Seeing that the sonic point is now over $1\,R_\odot$ further out with the MHD model, it is reasonable to place our new mass-loading region further out as well. However, with changes in location (and model) also come changes in wind density. Both factors cause the local solar wind density to decrease. For example, $\rho\,(5\,R_\odot)$ in the MHD model is nearly an order of magnitude less than $\rho\,(4\,R_\odot)$ in the HD model. It is no longer reasonable to use the same mass-loading rate $P_{\rm ml}$ value as with the HD model. We will instead select $P_{\rm ml}$ such that the ratio of the mass per volume being added to the solar wind over a fixed time and the initial local solar wind density remains about the same.

[19] Additionally, the spatial bounds on the mass-loading region need to be adjusted. As evidenced in Figure 2, wind velocities in the MHD model are dependent on the polar angle. We are only concerned with comparing the HD results with results originating from similar velocity profiles, so we also restrict our mass-loading region to the slow wind near the current sheet by placing bounds on the z coordinates. This results in a ring-shaped mass-loading region. Since we expect a shock to form in results involving postsonic point mass-loading regions, we also use AMR to create a similarly shaped refined grid encompassing any postsonic point mass-loading regions to help better resolve the shock.

[20] We solve equations (11)–(15) to find new steady states for two cases. One representing the presonic point 1-D results and the other representing the postsonic point results. $P_{\rm ml}$ is chosen for each case to scale appropriately with the local wind density in the 3-D MHD model. For the postsonic case, the mass-loading region is defined by a ring bounded by $7\,R_\odot \leq r \leq 8\,R_\odot$ and extending above and below by $1\,R_\odot$ in the z direction. The region is then refined appropriately, as seen in Figure 4. For the presonic point case we instead bound the mass-loading region in the radial direction by $4.5\,R_\odot \leq r \leq 5.5\,R_\odot$. Radial velocity and mean mass are plotted for both cases in Figure 5.

[21] The first difference to point out is purely due to our additional AMR region for the postsonic case. The two

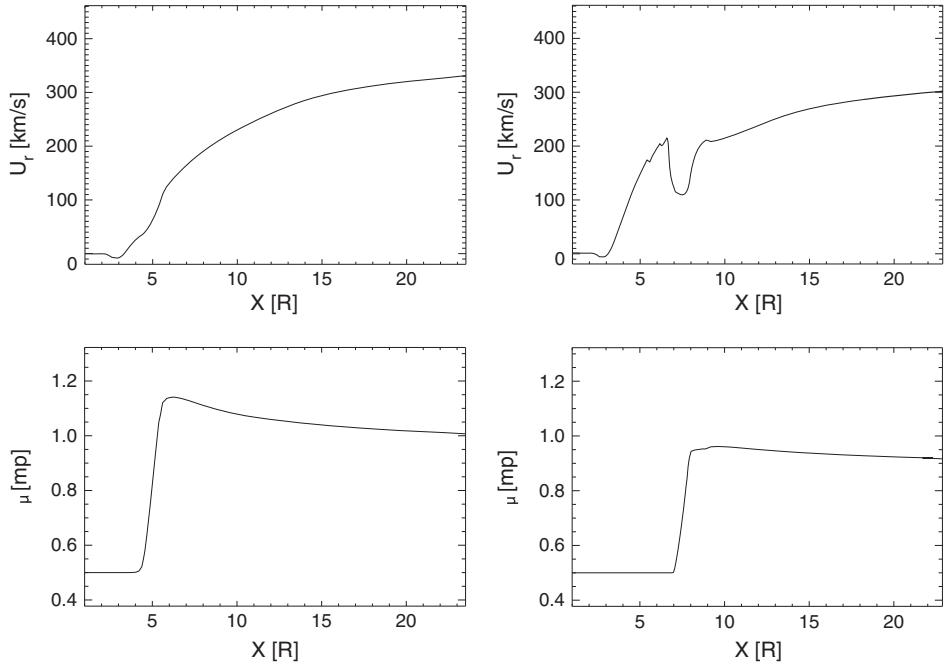

Figure 5. Velocity and mean mass profiles for the cases of mass-loading the solar wind (top) between $4.5\,R_\odot \leq r \leq 5.5\,R_\odot$ and (bottom) between $7\,R_\odot \leq r \leq 8\,R_\odot$. These correspond to similar cases in Figure 1 for mass-loading the solar wind before and after the sonic point.

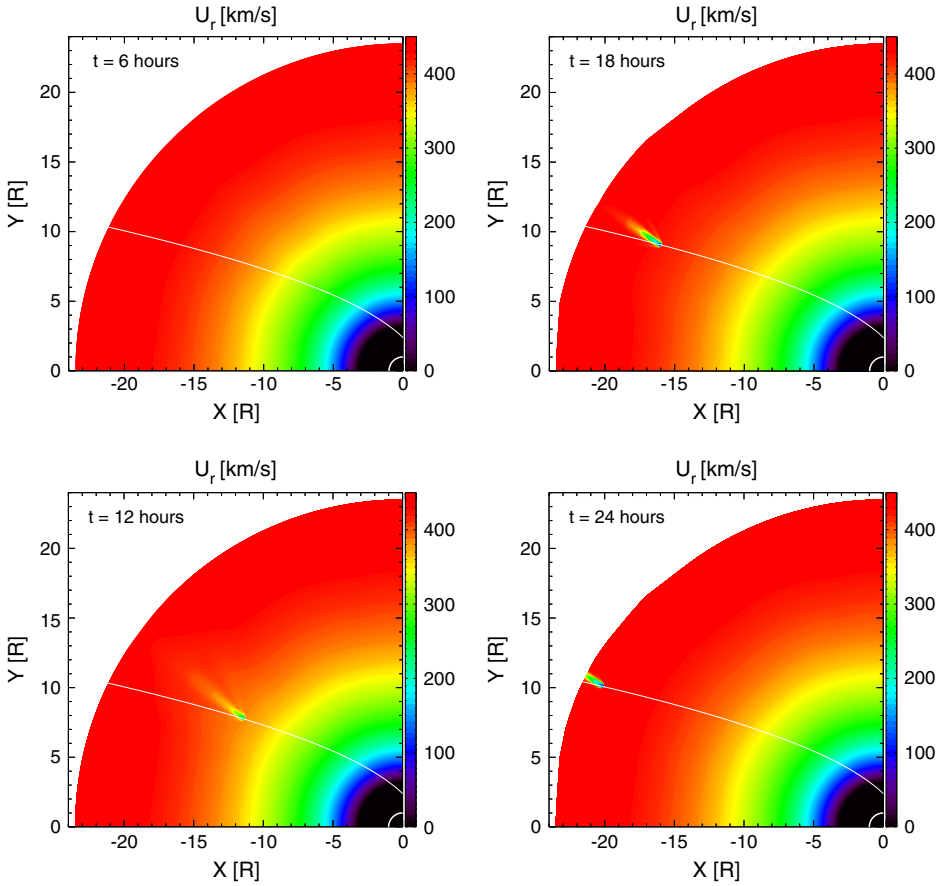

Figure 6. Radial velocity results from using the MHD coronal model to place a dust source along a sungrazing cometary orbit (white curve) in the *xy* plane, using a mass loss rate of 1.7×10^4 kg/s. The four panels correspond to 6, 12, 18, and 24 h after perihelion.

jumps preceding the shock in the velocity curve are nonphysical artifacts resulting from larger numerical errors generated at the boundary between grids of different resolution. This type of discontinuity is inherent in any discretization scheme with a nonuniform grid, and although their magnitude can be reduced, they cannot be completely removed from our solution. The same occurs when transitioning back to the coarser grid, though not as prominent. This can be seen in both velocity and mean mass curves.

[22] While the velocity profiles in Figure 5 share several similarities with Figure 1, such as the shock and reacceleration for the postsonic point case and upwind velocities reduction for the presonic point case, there are dramatic differences in the mean mass profiles proceeding the mass-loading region. In the HD model the greatest mean mass is accomplished with the mass-loading region that begins furthest out from the Sun, reaching approximately 0.75 m_p. The mean masses reached with the MHD model are not only much greater but the trend is reversed, with the presonic point mass-loading region resulting in a greater mean mass. A likely contributing factor is the lower undisturbed solar wind speed relative to the HD model, with an increasing difference closer to the Sun. The lower velocities are less effective at transporting ionized dust particles, allowing additional buildup in the mass-loading regions, though other factors may contribute to the increased mean mass.

5. Application: Sungrazing Comets

[23] In addition to particle migration to the F-corona, another way for dust to find its way into the corona, and thus be picked up by the solar wind, is through sungrazing comets that emit dust and gas near the Sun. Comets venturing in so close to the Sun can potentially lose significant mass from a single pass, if they survive at all. On 15 December 2011 the comet C/2011 W3 (Lovejoy) passed within $0.2\,R_\odot$ of the solar surface, significantly reducing its mass and leading to a cataclysmic fragmentation days later [*Sekanina and Chodas*, 2012]. Such a loss in mass should create very evident localized impacts to the wind velocity. Modeling solar wind mass-loading from a sungrazing comet such as C/2011 W3 serves as our first application of the mass-loading model a full 3-D MHD environment.

[24] With a functioning mass-loading component established, we move to approximating the mass-loading region as a single point source on the cometary path. However, when working with computational grids, we must settle for a single computational cell acting as our "point" source. This should be sufficient if the cell volume is comparable in size to a cometary coma, the dusty atmosphere that can range in size from 10^4 to 10^5 km across. In the extreme case of 2007's Comet 17P/Holmes, the coma expanded to a volume greater than the Sun. Images provided in *Sekanina and Chodas* [2012] and taken by *Černý* [2011]

show the head of C/2011 to be several times 10^4 km in width a day after perihelion.

[25] For the first simulations of our sungrazing comet application we place a dust source at various locations along a cometary path using the same orbital characteristics as C/2011 W3, but restricted to the equatorial plane, eliminating the need to add extra refinement outside the current sheet. *Sekanina and Chodas* [2012] provide orbital characteristic for C/2011 W3, which has a perihelion of $1.2\,R_\odot$. The comet takes over 2 days to pass through our solar corona domain and we will use $t = 0$ as the reference time for perihelion. At the locations selected along this path the grid will be refined such that the cell volume acting as our "point" source will be the same as a spherical coma with radius 10^4 km.

[26] In addition to orbital characteristics, we obtained dust loss estimates for Comet C/2011 from *Sekanina and Chodas* [2012]. Using postperihelion light curve data, they find an effective cross-sectional area X_d of the dust in the cloud. This is then used in their model to estimate the mass loss indicated by the scattered sunlight by dust particles of diameter d with a size distribution d^{-k},

$$M_d = \begin{cases} \frac{2(k-3)}{3(4-k)}\Theta\rho_{\text{bulk}}X_d d_{\text{min}}^{k-3}d_{\text{max}}^{4-k} & 3 < k < 4 \\ \frac{2(k-3)}{3(k-4)}\Theta\rho_{\text{bulk}}X_d d_{\text{min}} & k > 4 \end{cases}, \tag{24}$$

which is an overestimate due to the contribution of sodium ions in the light curve. Equation (24) is for a specific range in dust particle sizes, from d_{min} to d_{max}, and where $\rho_{\text{bulk}} = 0.4$ g cm^{-3} is the bulk dust density and Θ is the coefficient

$$\Theta = \frac{1-(d_{\text{min}}/d_{\text{max}})^{|k-4|}}{1-(d_{\text{min}}/d_{\text{max}})^{k-3}}. \tag{25}$$

Sekanina and Chodas [2012] state particles smaller than 0.1 μm that contribute very little to the mass, making $d_{\text{min}} = 0.1$ μm. For d_{max}, multiple values are used in their study, but we will set $d_{\text{max}} = 100$ μm since it is an upper limit for dust particles getting picked up by the solar wind, and $k = 3.5$, which also gives an upper estimate for the total mass. Due to the light curve being much stronger postperihelion than during preperihelion, the dust is presumed to be released during the 2 days between perihelion and the time of the cataclysmic fragmentation. With these parameters we have a total mass loss of approximately 3×10^9 kg over that time period.

[27] Simulations for modeling mass-loading due to a sungrazing comet are prepared in the following manner. We assume that the estimated mass loss of 3×10^9 kg is evenly distributed between $t = 0$ (perihelion) and $t = 48$ h, which gives a mass loss rate of about 1.7×10^4 kg/s. This mass loss rate will be used as the mass-loading rate in the specified computational cell. Then, for various points on the orbit between perihelion ($r = 1.2\,R_\odot$) and the edge of our domain ($r = 24\,R_\odot$), time-independent solutions are found using the specified mass-loading rate.

[28] Figure 6 shows solutions from four different times: 6, 12, 18, and 24 h after perihelion, which is located on the x axis at $x = 1.2\,R_\odot$. This source orbits counterclockwise in the xy plane, as viewed from above, and much like with our previous results, a sudden localized deceleration occurs, with reacceleration downwind. The panels start at $t = 6$ h since any effects much closer to the Sun will become lost due to the much higher solar wind density. For example, at $t = 6$ h, only minute changes can be seen in the velocity contours beyond $10\,R_\odot$. For $t = 18$ and $t = 24$ h, the resulting drop in velocity remained approximately the same, even though a drop in the solar wind density with increasing r should result in a more pronounced velocity change if the mass-loading rate remains constant.

6. Future Work

[29] This work provides an overview of our initial work adding a mass-loading component to a 3-D MHD corona model based on BATS-R-US as means to model interplanetary dust being picked up by the solar wind. Results from the 1-D HD and 3-D MHD models are similar, but there exist some noticeable differences. Additionally, obtaining the predicted results for dust-producing cometary sources based on 1-D and 3-D results shows that this model can be used for various types of mass-loading events, leading to results comparable with observations from Solar Probe Plus.

[30] Work with our cometary application is still in the beginning stages, with several ways to improve beyond a single "point" source. Dust particles shed from comets may not be picked up right at the source, but may survive on trajectories that form the dust tail. *Mendis et al.* [1985] describes the framework for the distribution of dust particle in the dust tail, based on calculating trajectories of released dust particles of various sizes. From these new trajectories for particles of various sizes and release times, sets of curves called syndynes and synchrones can be computed to determine the shape of the dust tail. Our next step with regards to the cometary application is to use this syndyne- and synchrone-defined area as our mass-loading region.

[31] **Acknowledgments.** This work utilized the Janus supercomputer, which is supported by the National Science Foundation (award CNS-0821794) and the University of Colorado Boulder. The Janus supercomputer is a joint effort of the University of Colorado Boulder, the University of Colorado Denver, and the National Center for Atmospheric Research. Janus is operated by the University of Colorado Boulder. Additionally, we would like to thank R. Oran, B. van der Holst, T. Gombosi, and G. Tóth of the University of Michigan's Center for Space Environment Modeling for providing help with SC component of the SWMF.

[32] Philippa Browning thanks the reviewers for their assistance in evaluating this paper.

References

Arge, C. N., and V. J. Pizzo (2000), Improvement in the prediction of solar wind conditions using near-real time solar magnetic field updates, *J. Geophys. Res.*, *105*, 10,465–10,480.

Biermann, L., B. Brosowski, and H. U. Schmidt (1967), The interaction of the solar wind with a comet, *Solar Phys.*, *1*, 254–284.

Černý, J. (2011), http://www.kommet.cz/page.php?al=prvni_\snimky_komety_lovejoy_ze_zeme.

Gombosi, T. I., A. F. Nagy, and T. E. Cravens (1986), Dust and neutral gas modeling of the inner atmosphere of comets, *Rev. Geophys.*, *24*, 667–700.

Grün, E., M. Horányi, and Z. Sternovsky (2011), The lunar dust environment, *Planet. Space Sci.*, *59*, 1672–1680.

Hollweg, J. V. (1986), Transition region, corona, and solar wind in coronal holes, *J. Geophys. Res.*, *91*, 4111–4125.

Horány, M. (1996), Charged dust dynamics in the solar system, *Annu. Rev. Astrophys.*, *34*, 383–418.

Horányi, M., et al. (2008), The student dust counter on the new horizons mission, *Space Sci. Rev.*, *140*, 387–402.

Mann, I., and R. H. MacQueen (1996), Observation and analysis of the F-corona brightness, *Adv. Space Res.*, *17*, 353–356.

Mendis, D. A., H. L. F. Houpis, and M. L. Marconi (1985), The physics of comets, *Fund. Cosmic Phys.*, *10*, 1–380.

Meyer-Vernet, N., M. Maksimovic, A. Czechowski, I. Mann, I. Zouganelis, K. Goetz, M. L. Kaiser, O. C. St. Cyr, J. L. Bougeret, and S. D. Bale (2009), Dust detection by the wave instrument on STEREO: Nanoparticles picked up by the solar wind?, *Solar Phys.*, *256*, 463–474.

Rasca, A. P., and M. Horányi (2013), Solar wind mass-loading due to dust, *AIP Conf. Proc.*, *1539*, 418–421.

Sekanina, Z., and P. W. Chodas (2012), Comet C/2011 W3 (Lovejoy): Orbit determination, outbursts, disintegration of nucleus, dust-tail morphology, and relationship to new cluster of bright sungrazers, *Astrophys. J.*, *757*, 127.

Tóth, G., et al. (2012), Adaptive numerical algorithms in space weather modeling, *J. Comp. Phys.*, *231*, 870–903.

van der Holst, B., W. B. Manchester, R. A. Frazin, A. M. Vásquez, G. Tóth, and T. I. Gombosi (2010), A data-driven, two-temperature solar wind model with Alfvén waves, *Astrophys. J.*, *725*, 1373–1383.